

A Faithful Deep Sensitivity Estimation for Accelerated Magnetic Resonance Imaging

Zi Wang[#], Haoming Fang[#], Chen Qian, Boxuan Shi, Lijun Bao, Lihong Zhu, Jianjun Zhou, Wenping Wei, Jianzhong Lin, Di Guo, and Xiaobo Qu^{*}

Abstract—Recent deep learning is superior in providing high-quality images and ultra-fast reconstructions in accelerated magnetic resonance imaging (MRI). Faithful coil sensitivity estimation is vital for MRI reconstruction. However, most deep learning methods still rely on pre-estimated sensitivity maps and ignore their inaccuracy, resulting in the significant quality degradation of reconstructed images. In this work, we propose a Joint Deep Sensitivity estimation and Image reconstruction network, called JDSI. During the image artifacts removal, it gradually provides more faithful sensitivity maps, leading to greatly improved image reconstructions. To understand the behavior of the network, the mutual promotion of sensitivity estimation and image reconstruction is revealed through the visualization of network intermediate results. Results on *in vivo* datasets and radiologist reader study demonstrate that, the proposed JDSI achieves the state-of-the-art performance visually and quantitatively, especially when the accelerated factor is high. Additionally, JDSI owns nice robustness to abnormal subjects and different number of autocalibration signals.

Index Terms—deep learning, parallel imaging, image reconstruction, magnetic resonance imaging

I. INTRODUCTION

MAGNETIC resonance imaging (MRI) is a leading non-invasive and non-radioactive diagnostic modality in modern medical science [1]. However, MRI scans usually require long time cost, and thus fast MRI technology attracts extensive research interests [2]. Parallel imaging [3, 4] is a widely used multi-coil acceleration technique in clinical systems, while sparse sampling [2, 5] provides a complementary scheme for further obtaining higher acceleration factor (AF).

Over the past two decades, coil correlation modeling has always been a key issue in advanced MRI reconstructions, which can be categorized into explicit and implicit sensitivity estimations. The former typically pre-acquires or pre-estimates the sensitivity maps from the autocalibration signal (ACS) [3, 6], and further applies sparse regularizations [2, 7-11] to coil-combined images to reduce the reconstruction error. Moreover,

sensitivity maps could also be regularized using polynomial functions [12], so as to continuously update the sensitivity estimation with the image reconstruction. For implicit methods, two main strategies include the k-space kernel learning [4, 13] and structured low rank [5, 14-16]. Recently, based on their good reconstruction performance and complementarity, the two approaches have been combined for further improvement [17, 18].

At present, deep learning has demonstrated their superior performance in fast MRI on excellent image quality and reconstruction speed [19-22]. Like conventional methods, there are also implicit and explicit strategies for deep learning when dealing with multi-coil data. Several implicit methods utilize multiple convolutional layers to achieve k-space interpolation [23-25]. Whereas most existing deep learning methods involve explicit sensitivity maps [26-29] generated from the pre-acquisition or pre-estimation using ESPIRiT [6].

When the AF is high or ACS lines are limited, the conventional sensitivity estimation will be inaccurate, and the error may affect the image reconstruction and bring significant image degradation [12, 14]. To overcome this problem, one interesting attempt is to estimate sensitivity maps through a deep network and then use them to conduct a conventional SENSE reconstruction [30]. To avoid pre-estimating, another work employs a U-Net as the sensitivity estimator and inserts it at the beginning of the network [31]. Through a joint image and sensitivity reconstruction network, these sensitivity maps can be updated with conventional linear operations [32]. Their promising results arouse our interest. Our further comparison found that these methods still need to be improved to achieve lower reconstruction error and better network interpretability (See Section IV).

A faithful sensitivity estimation is important for the high-quality MRI reconstruction using explicit methods [6, 12, 30]. In this paper, the ground truth of coil sensitivity maps is obtained via dividing the individual fully-sampled coil image

This work was supported in part by the National Natural Science Foundation of China under grants 62122064, 61971361, 61871341, and 62071405, the Natural Science Foundation of Fujian Province of China under grant 2021J011184, the President Fund of Xiamen University under grant 0621ZK1035, and the Xiamen University Nanqiang Outstanding Talents Program. ([#]Contributed equally to this work. ^{*}Corresponding author: Xiaobo Qu, email: quxiaobo@xmu.edu.cn)

Zi Wang, Haoming Fang, Chen Qian, Boxuan Shi, Lijun Bao, and Xiaobo Qu are with the Department of Electronic Science, Biomedical Intelligent Cloud R&D Center, Fujian Provincial Key Laboratory of Plasma and Magnetic Resonance, National Institute for Data Science in Health and Medicine, Xiamen University, Xiamen, China.

Lihong Zhu and Jianjun Zhou are with the Department of Radiology, Zhongshan Hospital (Xiamen), Fudan University, Xiamen, China.

Wenping Wei is with the Department of Radiology, The First Affiliated Hospital of Xiamen University, Xiamen, China.

Jianzhong Lin is with the Department of Radiology, Zhongshan Hospital affiliated to Xiamen University, Xiamen, China.

Di Guo is with the School of Computer and Information Engineering, Xiamen University of Technology, Xiamen, China.

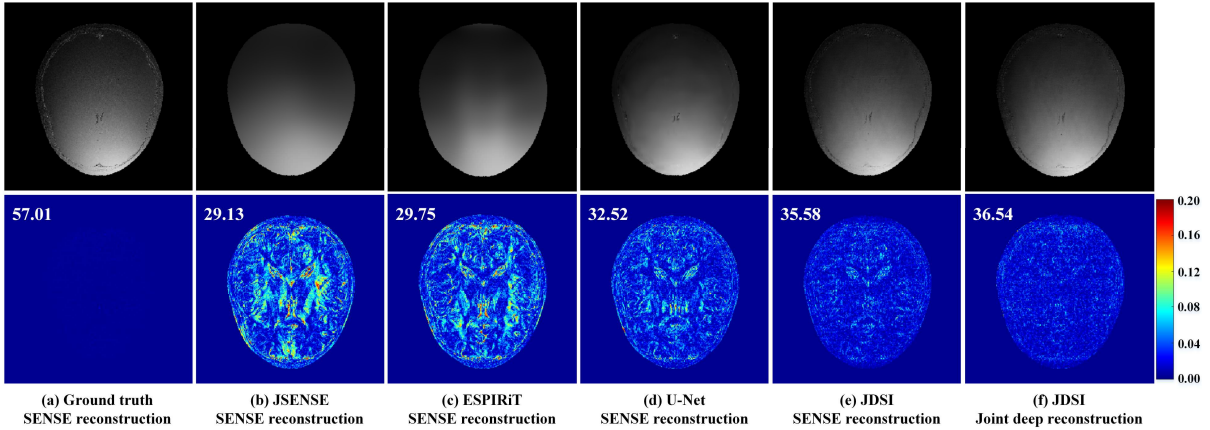


Fig. 1. Brain image reconstructions under a 1D Cartesian undersampling pattern with AF=6. First row: (a) Ground truth of 14th coil which is generated via dividing the individual fully-sampled coil image by the sum of squares (SoS) image of fully-sampled multi-coil images. Estimated sensitivity maps using (b) JSENSE [12], (c) ESPIRiT [6], (d) U-Net [31], and (e)-(f) the proposed method. Second row: (a)-(e) Reconstruction errors using SENSE-based reconstruction [11] and (f) the proposed joint deep reconstruction. Note: PSNR(dB) is listed for each reconstruction.

by the sum of squares (SoS) of fully-sampled multi-coil images. With these ground truth sensitivity maps, Fig. 1(a) illustrates that an almost error-free reconstruction can be achieved. In contrast, the estimated sensitivity maps that more approximate to the ground truth have better SENSE-based reconstructions [11] (Figs. 1(b)-(e)). And our proposed joint deep learning can further suppress artifacts (Fig. 1(f)). This example clearly shows that a better sensitivity map leads to a lower reconstruction error, no matter for the conventional or deep learning methods.

Our joint deep network, called JDSI, is proposed to simultaneously achieve the faithful estimation of sensitivity maps and reconstruction of high-quality images. The main contributions are summarized as follows:

1) We design a sensitivity estimation module to refine sensitivity maps during image reconstructions. Remarkably, it uses all measured k-space rather than only ACS lines, to estimate more faithful sensitivity maps.

2) We explain our network by visualizing the intermediate sensitivity maps and images. It is found that the alternating sensitivity estimation and image artifacts removal promote each other, leading to high-quality reconstructions.

3) Extensive results on *in vivo* brain datasets show that, the proposed JDSI provides superior reconstruction performance under both objective criteria and experienced radiologists' evaluations.

The remainder of this paper is organized as follows. Section II formulates the problem of MRI reconstruction. Section III describe the proposed method and its implementation details. Section IV shows experiment details and results. Section V and VI provide discussions and the conclusion, respectively.

II. PROBLEM FORMULATION

Magnetic resonance image reconstruction problem is to recover a desired image $\mathbf{x} \in \mathbb{C}^N$ from the measured multi-coil k-space $\mathbf{y} \in \mathbb{C}^{JN}$ which is undersampled by an operator \mathcal{U} with non-acquired positions zero-filled. The forward model can be defined as

$$\mathbf{y} = \mathcal{U}\mathbf{F}\mathbf{S}\mathbf{x} + \boldsymbol{\varepsilon}, \quad (1)$$

where $\mathbf{S} = [\mathbf{S}_1; \dots; \mathbf{S}_j; \dots; \mathbf{S}_J] \in \mathbb{C}^{JN \times N}$ is the set of sensitivity maps. N represents the dimension of the vectorized image and J is the number of coils. $\mathbf{S}_j \in \mathbb{C}^{N \times N}$ is a diagonal matrix which denotes the sensitivity map of the j^{th} coil. \mathcal{F} is the Fourier transform, $\boldsymbol{\varepsilon} \in \mathbb{C}^{JN}$ is the additive Gaussian noise.

For this ill-posed problem in Eq. (1), assuming that the sensitivity maps \mathbf{S} are pre-acquired or pre-calculated from the ACS region, it can be solved using the following optimization model with a regularization term $\mathcal{R}_1(\cdot)$, e.g. the l_1 -norm in image sparsity [2, 7-11]):

$$\min_{\mathbf{x}} \frac{1}{2} \|\mathbf{y} - \mathcal{U}\mathbf{F}\mathbf{S}\mathbf{x}\|_2^2 + \mathcal{R}_1(\mathbf{x}). \quad (2)$$

However, the pre-estimated sensitivity maps may not be accurate due to inconsistent pre-scan or limited ACS lines [12]. Then, inaccuracy sensitivity estimation will affect the image reconstruction and resulting in artifacts [24, 30].

To improve the sensitivity estimation, a joint sensitivity estimation and image reconstruction model is proposed [12]. It simultaneously updates the sensitivity maps and image. After introducing another regularization term of the sensitivity maps $\mathcal{R}_2(\cdot)$ (e.g., polynomial regularization [12]), Eq. (2) is extended as:

$$\min_{\mathbf{x}, \mathbf{S}} \frac{1}{2} \|\mathbf{y} - \mathcal{U}\mathbf{F}\mathbf{S}\mathbf{x}\|_2^2 + \mathcal{R}_1(\mathbf{x}) + \mathcal{R}_2(\mathbf{S}). \quad (3)$$

To solve the optimization problem in Eq. (3), the conventional reconstruction methods update \mathbf{S} and \mathbf{x} alternatively, until the convergence [12]. The reconstruction process is time-consuming due to the usage of an iterative optimization algorithm, while the regularization constraints and their parameters need to be manually determined.

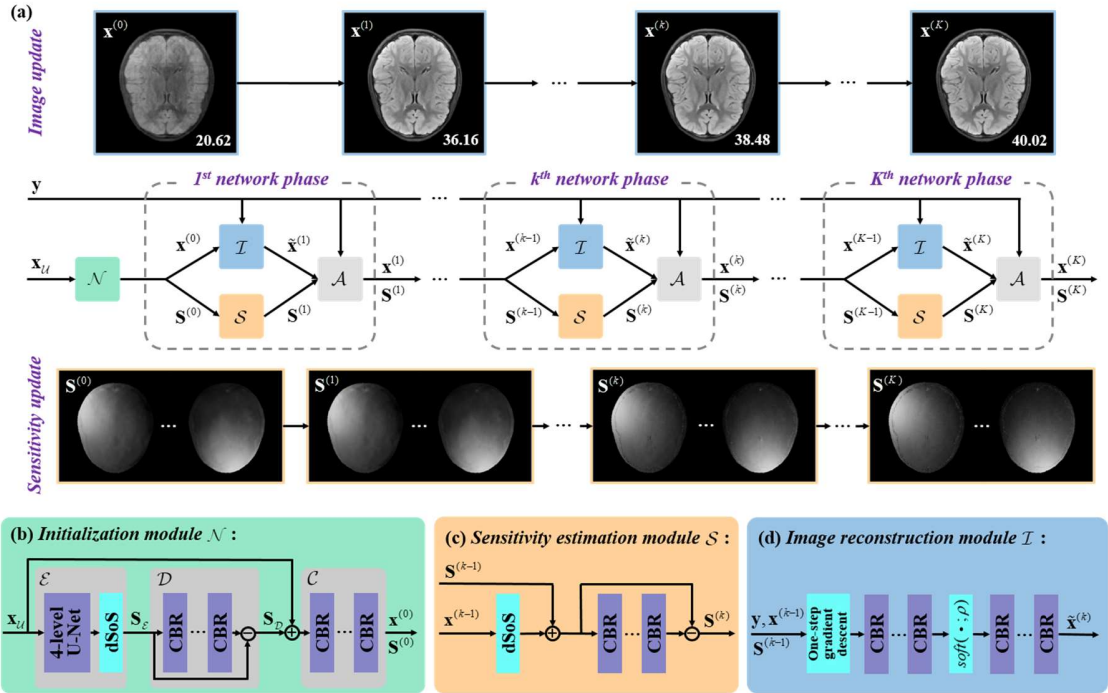


Fig. 2. The proposed JDSI for accelerated MRI. (a) The recursive JDSI architecture includes (b) initialization module \mathcal{N} , (c) sensitivity estimation module \mathcal{S} , (d) image reconstruction module \mathcal{I} , and data consistency module \mathcal{A} . Note: “CBR” is the convolution, batch normalization, and ReLU. “dSoS” is the operation that divided by the sum of squares images. PSNR(dB) is listed in each reconstructed image.

III. PROPOSED METHOD

In this section, we propose a joint deep network whose architecture is inspired by the alternating iterative idea of the conventional reconstruction. Then, the detailed network implementation is presented.

A. JDSI: Joint Deep Sensitivity Estimation and Image Reconstruction Network

Here, we propose a Joint Deep Sensitivity estimation and Image reconstruction network (JDSI) to alternate between updating \mathbf{S} and \mathbf{x} , using a deep learning scheme. Their updates correspond to two network modules, i.e., sensitivity estimation module \mathcal{S} and image reconstruction module \mathcal{I} . An initialization module is also integrated at the network beginning to provide proper initialized image and sensitivity maps. Besides, to ensure the network reconstructions are aligned to the acquired data, the data consistency module is added.

Fig. 2 gives the network architecture of our proposed JDSI. Specifically, our network firstly estimates initialized sensitivity maps from the undersampled multi-coil k-space and provides the initialized coil-combined image. Second, the sensitivity estimation module is utilized to refine sensitivity maps from whole multi-coil k-space. Third, the undersampling artifacts are removed through the image reconstruction module. Fourth, reconstructed images and sensitivity maps are projected back to the k-space and then forced to maintain the data consistency to the acquired k-space measurements. After repeating the last three modules K times, the final reconstructed image can be obtained.

1) Initialization module

Fig. 2(b) is the initialization module that aims to initialize sensitivity maps and the coil-combined image. We employ three sub-networks (i.e., $\mathcal{E}, \mathcal{D}, \mathcal{C}$), to obtain initial sensitivity maps $\mathbf{S}^{(0)}$ from undersampled multi-coil image $\mathbf{x}_U = \mathcal{F}^* \mathcal{U}^* \mathbf{y}$. The overall process is written as

$$\mathbf{S}^{(0)} = \mathcal{N}(\mathbf{x}_U; \boldsymbol{\theta}_{\mathcal{N}}), \quad (4)$$

where $\boldsymbol{\theta}_{\mathcal{N}}$ is the network parameters for the mapping \mathcal{N} . The superscript $*$ represents the adjoint operation. Three sub-networks are defined as

$$\begin{cases} \mathbf{S}_{\mathcal{E}} = \mathcal{E}(\mathbf{x}_U; \boldsymbol{\theta}_{\mathcal{E}}) \\ \mathbf{S}_{\mathcal{D}} = \mathcal{D}(\mathbf{S}_{\mathcal{E}}; \boldsymbol{\theta}_{\mathcal{D}}) \\ \mathbf{S}^{(0)} = \mathcal{C}(\mathbf{S}_{\mathcal{D}}, \mathbf{x}_U; \boldsymbol{\theta}_{\mathcal{C}}) \end{cases}, \quad (5)$$

where $\boldsymbol{\theta}_{\mathcal{E}}, \boldsymbol{\theta}_{\mathcal{D}}, \boldsymbol{\theta}_{\mathcal{C}}$ are the network parameters for the mapping $\mathcal{E}, \mathcal{D}, \mathcal{C}$, respectively. Through an encoder-decoder network \mathcal{E} , the undersampled image \mathbf{x}_U is obtained with just low-resolution information, then sensitivity maps $\mathbf{S}_{\mathcal{E}}$ are generated via dividing the individual coil images by the sum of squares (SoS) image [31]. Unlike those methods [6, 30] that only use the ACS region to get low-resolution sensitivity maps, we exploit the whole acquired k-space to capture more high-frequency information [12]. A denoiser \mathcal{D} is followed to remove the residual noises and artifacts, then the denoised sensitivity maps $\mathbf{S}_{\mathcal{D}}$ are obtained. Finally, a network \mathcal{C} is employed to extract sensitivity features from the fusion of

undersampled image \mathbf{x}_U and \mathbf{S}_D to generate initial sensitivity maps $\mathbf{S}^{(0)}$.

Once the initialized sensitivity maps $\mathbf{S}^{(0)}$ are generated, the initialized coil-combined image can be obtained as $\mathbf{x}^{(0)} = (\mathbf{S}^{(0)})^* \mathbf{x}_U$, whereas may be with strong artifacts.

2) Sensitivity estimation module

Fig. 2(c) is the sensitivity estimation module that corresponds to update \mathbf{S} , which inputs are the fusion of $\mathbf{x}^{(k-1)}$ and $\mathbf{S}^{(k-1)}$:

$$\mathbf{S}^{(k)} = \mathcal{S}(\mathbf{x}^{(k-1)}, \mathbf{S}^{(k-1)}; \boldsymbol{\theta}_S), \quad (6)$$

where k denotes the number of network phase, and $\boldsymbol{\theta}_S$ is the network parameters for the mapping \mathcal{S} . The mapping is a multi-layer convolutional network to refine the sensitivity maps for their improved estimation. In this way, more texture information can be retained to further approximate the ground truth sensitivity maps. It prevents the errors of the estimated sensitivities from propagating to the final reconstruction.

3) Image reconstruction module

Fig. 2(d) is the image reconstruction module that corresponds to update \mathbf{x} . Since this module is designed for artifacts removal, here, we utilize the efficient deep thresholding network [25, 28, 33, 34]:

$$\tilde{\mathbf{x}}^{(k)} = \mathcal{I}(\mathbf{x}^{(k-1)} - \gamma(\mathbf{S}^{(k-1)})^* \mathcal{F}^* \mathcal{U}^* (\mathcal{U} \mathcal{F} \mathbf{S}^{(k-1)} \mathbf{x}^{(k-1)} - \mathbf{y}); \boldsymbol{\theta}_I), \quad (7)$$

where $\boldsymbol{\theta}_I$ is the network parameters for the mapping \mathcal{I} . γ is set as a learnable parameter initialized to 1. The mapping involves two multi-layer convolutional networks, and an element-wise soft-thresholding $\text{soft}(x; \rho) = \max\{|x| - \rho, 0\} \cdot x/|x|$ is inserted between them, where ρ is the learnable threshold that is initialized to 0.001 and varies at each network phase.

4) Data consistency module

In this module, each final output is forced to maintain the data consistency to the measured k-space:

$$\mathbf{x}^{(k)} = \mathcal{A}(\tilde{\mathbf{x}}^{(k)}, \mathbf{S}^{(k)}; \mathbf{y}; \lambda), \quad (8)$$

where $\tilde{\mathbf{x}}^{(k)}$ and $\mathbf{S}^{(k)}$ are the output of the image reconstruction and sensitivity estimation module, respectively. λ is a learnable trade-off parameter initialized as 10^6 . Specifically, it is defined as

$$(\mathcal{F}^* \mathbf{S}^{(k)} \mathbf{x}^{(k)})_n = \begin{cases} (\mathcal{F}^* \mathbf{S}^{(k)} \tilde{\mathbf{x}}^{(k)})_n, & n \notin \Omega \\ \left(\frac{\mathcal{F}^* \mathbf{S}^{(k)} \tilde{\mathbf{x}}^{(k)} + \lambda \mathbf{y}}{1 + \lambda} \right)_n, & n \in \Omega \end{cases}, \quad (9)$$

where n is the index and Ω is the set of the sampled positions in k-space. Eq. (9) implies that, at the sampled positions, the points should maintain a trade-off with \mathbf{y} , while the update of the unsampled points depends entirely on the reconstruction results of the network.

5) Network interpretability

To demonstrate the network interpretability of JDSI, in Fig. 2(a), we visualized the intermediate sensitivity maps and the corresponding reconstructed images.

With the increase of the network phase, the alternating sensitivity estimation and image de-aliasing promote each other. The sensitivity maps gradually approximate the ground truth,

while image artifacts are gradually removed. This enables our network to obtain faithful sensitivity maps and benefits high-quality image reconstruction.

B. Network Architecture and Loss Function

As shown in Fig. 2, the proposed JDSI is an unrolled recursive network, where the number of total network phase K is set as 5 to trade-off between the reconstruction performance and time consumption.

Our network architecture is as follows: (1) Initialization module has three sub-networks. Encoder-decoder network \mathcal{E} is a modified 4-level U-Net [35] and the number of filters grows from 32 to a maximum of 256. Denoiser \mathcal{D} and sensitivity extraction network \mathcal{C} consist 15 and 5 convolutional layers, respectively, and each layer contains 64 filters, followed by batch normalization and ReLU. (2) Sensitivity estimation module is a 5-layer convolutional denoiser, and each layer contains 64 filters, followed by batch normalization and ReLU. (3) Image reconstruction module \mathcal{I} involves an element-wise soft-thresholding and two 4-layer convolutional networks. Each layer contains 32 filters, followed by batch normalization and ReLU. Besides, the size of all convolutional filters in our network is 3×3 , and the input and output channels of all sub-networks are adjusted according to the number of data coils.

The network weights are Xavier initialized and trained for 200 epochs with the Adam optimizer. Their initial learning rate is set to 0.001 with an exponential decay of 0.99. The batch size is 2. The loss function of the proposed JDSI is defined as:

$$\mathcal{L} = \mathcal{L}_{coil} + \alpha_1 \mathcal{L}_{combine} + \alpha_2 \mathcal{L}_{sensitivity} \\ = \frac{1}{KT} \sum_{k=1}^K \sum_{t=1}^T \left(\left\| \mathbf{x}_t^{ref} - \mathbf{S}_t^{(K)} \mathbf{x}_t^{(K)} \right\|_2^2 + \left(\alpha_1 \left\| (\mathbf{S}_t^{ref})^* \mathbf{x}_t^{ref} - \mathbf{x}_t^{(K)} \right\|_2^2 + \alpha_2 \left\| \mathbf{S}_t^{ref} - \mathbf{S}_t^{(K)} \right\|_2^2 \right) \right), \quad (10)$$

where T is the number of training samples. α_1, α_2 are set as 0.1 and 0.1, respectively. $\mathcal{L}_{coil}, \mathcal{L}_{combine}, \mathcal{L}_{sensitivity}$ are the multi-coil image loss, combined-coil image loss, and sensitivity map loss, respectively. \mathbf{x}_t^{ref} is the fully-sampled multi-coil image of the t^{th} training sample. \mathbf{S}_t^{ref} denote the ground truth sensitivity maps.

The proposed network was implemented on a server equipped with dual Intel Xeon Silver 4210 CPUs, 128 GB RAM, and the Nvidia Tesla T4 GPU (16 GB memory) in Tensorflow 2.2.0. The typical training of JDSI took about 16 hours.

IV. EXPERIMENTAL RESULTS

A. Datasets and Evaluation Criteria

Two brain datasets from the fastMRI dataset [36] were used in this paper. They were axial T2 FLAIR and T2 weighted k-space data. The former: We selected 32 subjects and each subject contained about 16 slices of size $320 \times 320 \times 16$. 26 subjects were used for training and the remaining for test. The latter: We selected 37 subjects and each subject contained about 20 slices of size $320 \times 320 \times 16$. 30 subjects were used for training and the remaining for test. All datasets were fully sampled, and

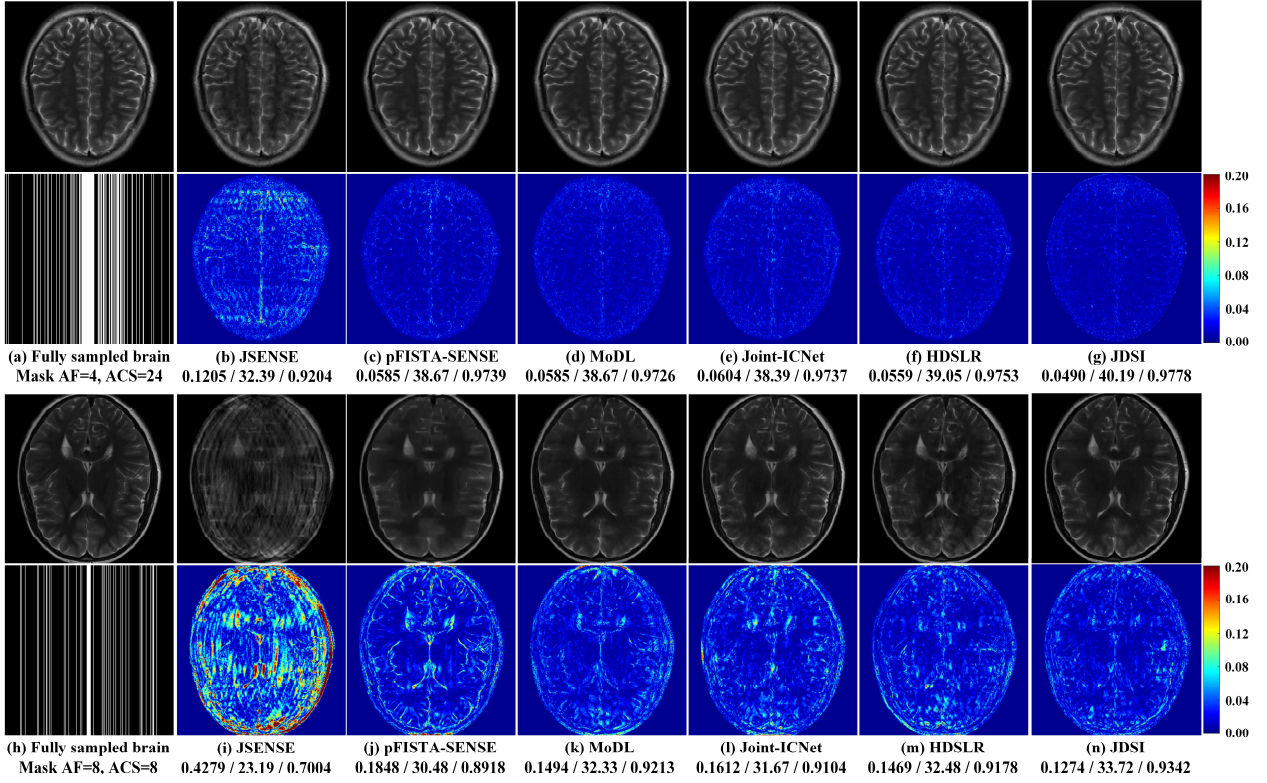


Fig. 3. Calibration-based reconstruction results of the T2 weighted brain dataset using different methods. (a) (or (h)) is the fully sampled image and the 1D Cartesian undersampling pattern with AF=4 (or AF=8). (b)-(g) (or (i)-(n)) are reconstructed images and the corresponding error maps. Note: RLNE/PSNR(dB)/SSIM are listed for each reconstruction.

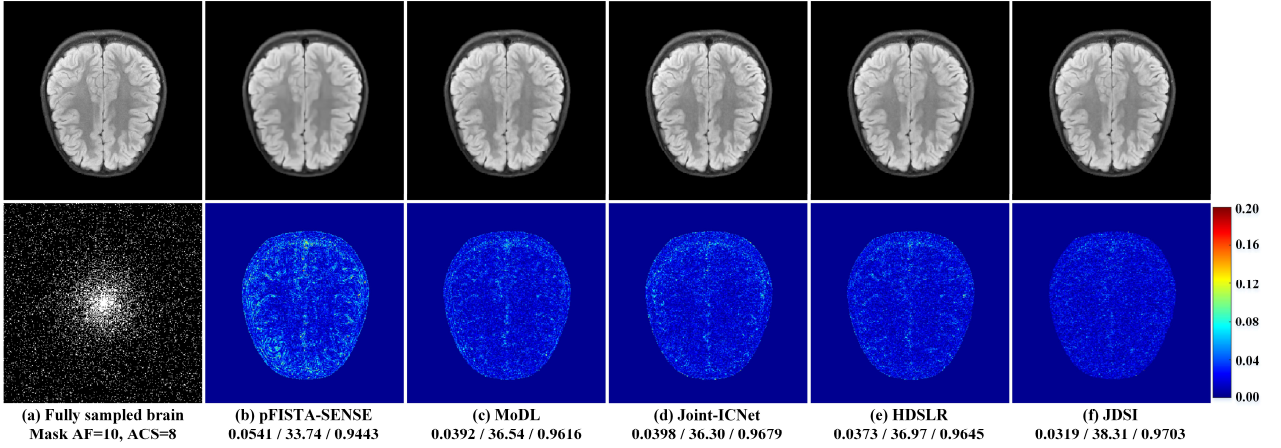


Fig. 4. Calibration-based reconstruction results of the T2 FLAIR brain dataset using different methods. (a) is the fully sampled image and the 2D random undersampling pattern with AF=10. (b)-(e) are reconstructed images and the corresponding error maps. Note: RLNE/PSNR(dB)/SSIM are listed for each reconstruction.

they were retrospectively undersampled for training and test.

To quantitatively evaluate the reconstruction performance, we utilized three evaluation criteria: The relative l_2 norm error (RLNE) [9], peak signal-to-noise ratio (PSNR), and structural similarity index (SSIM) [37]. The lower RLNE, higher PSNR, and higher SSIM indicate lower reconstruction error, less image distortions, and better details preservation, respectively.

B. Evaluation of Calibration-based Reconstruction

To validate the advantages of the proposed JDSI, we first compared it with the state-of-the-art methods under common

calibration-based undersampling patterns. These patterns have fully-sampled center ACS regions for sensitivity encoding or k-space kernel learning, to model the relationship between multiple coils.

For comparison study, conventional parallel imaging method JSENSE [12] was used as the reconstruction baseline (Only supports 1D undersampling). We also compared the state-of-the-art reconstruction method pFISTA-SENSE [11], and three deep learning methods including MoDL [27], Joint-ICNet [32], and HDLSR [24]. JSENSE is a classical joint sensitivity estimation and image reconstruction method. pFISTA-SENSE

and MoDL need pre-estimate sensitivity maps using ESPIRiT [6]. Joint-ICNet is a joint method but update sensitivity maps using conventional linear operation. HDLSR, like the proposed JDSI, does not rely on the ACS region. Parameters of all conventional methods was optimized to obtain the lowest RLNE. The network phase of Joint-ICNet was set as 5 due to GPU memory limitation (16GB). Other deep learning methods were executed according to typical settings mentioned by the authors.

For 1D undersampling, Figs. 3(a)-(g) show that, when the acceleration factor is low (AF=4), except JSENSE has obvious artifacts, other compared methods provide the images with nice artifacts suppression while JDSI achieves best performance visually and quantitatively. However, when the acquisition is highly accelerated (AF=8), all compared methods own dramatic degradation and yield results exhibiting obvious artifacts, whereas JDSI has smallest reconstruction error and outperforms them about 1.24~10.53dB in PSNR (Figs. 3(h)-(n)).

For 2D undersampling, Figs. 4(a)-(f) show that, JDSI provides best reconstructions, while compared methods have edge artifacts and details blurring. Consistent quantitative comparisons of more datasets are summarized in Table I.

These results demonstrate that, for calibration-based reconstruction, JDSI can achieve the best ability of the artifacts suppression and details preservation, under different tested undersampling patterns and acceleration factors.

C. Evaluation of Calibrationless Reconstruction

In general, the need to obtain ACS signals prolongs the overall data acquisition time and sometimes increases the susceptibility to subject motion [14-16]. Therefore, calibrationless reconstruction has become a research hotspot due to it does not rely on ACS signals [14-16, 24, 25]. Different to other sensitivity-based methods, our proposed JDSI estimates and updates the sensitivity maps from the whole k-space instead of the center ACS region, leading to a potential for successful calibrationless reconstruction. Here, we compared the proposed JDSI with the state-of-the-art calibrationless methods.

For comparison study, two representative low-rank modeling methods P-LORAKS [16] and SAKE [14] were included. Both methods iteratively interpolate k-space through structured low-rank matrix. Besides, a calibrationless deep learning method HDLSR [24] was also compared. Parameters of all conventional methods was optimized to obtain the lowest RLNE. The deep learning method was executed according to the typical setting mentioned by the authors.

Calibrationless reconstruction is more challenging than the former calibration-based reconstruction. As expected, the results shown in Fig. 5 and Table II are worse than that in the patterns with ACS signals. Interestingly, consistent with the previous results, the proposed JDSI still outperforms all compared methods visually and quantitatively in both 1D and 2D undersampling. HDLSR performs well on the 1D pattern, but yields obvious artifacts and image blurring on the 2D pattern. Both two low-rank methods do not achieve satisfactory images on the tested undersampling patterns.

These results demonstrate that, for calibrationless reconstruction, JDSI can still obtain lowest reconstruction error and highest structural similarity under different tested undersampling patterns and acceleration factors, again suggesting its effectiveness and flexibility.

TABLE I

RLNE ($\times 10^{-2}$)/PSNR (dB)/SSIM ($\times 10^{-2}$) OF BRAIN RECONSTRUCTIONS UNDER CALIBRATION-BASED UNDERSAMPLING PATTERNS [MEAN \pm STD].

1D Cartesian undersampling pattern (AF=4, ACS=24)					
Dataset	Method	RLNE	PSNR	SSIM	
T2 weighted	JSENSE	12.62 \pm 1.58	30.97 \pm 1.14	90.25 \pm 1.92	
	pFISTA-SENSE	6.53 \pm 1.48	36.93 \pm 1.39	96.28 \pm 1.27	
	MoDL	6.52 \pm 1.46	36.82 \pm 1.42	96.29 \pm 0.97	
	Joint-ICNet	7.20 \pm 1.47	35.93 \pm 1.37	95.93 \pm 1.46	
	HDLSR	6.13 \pm 1.42	37.37 \pm 1.44	96.53 \pm 1.24	
T2 FLAIR	JDSI	6.07\pm1.80	37.56\pm1.86	96.39\pm1.71	
	JSENSE	9.95 \pm 1.52	31.39 \pm 1.98	89.40 \pm 2.11	
	pFISTA-SENSE	6.53 \pm 1.28	35.12 \pm 1.75	94.78 \pm 1.25	
	MoDL	5.34 \pm 1.06	36.88 \pm 1.81	96.53 \pm 0.83	
	Joint-ICNet	4.68 \pm 0.80	37.97 \pm 1.97	96.65 \pm 0.88	
T2 FLAIR	HDLSR	4.44 \pm 0.83	38.46 \pm 2.22	97.03 \pm 0.83	
	JDSI	3.99\pm0.79	39.38\pm2.19	97.36\pm0.82	
	1D Cartesian undersampling pattern (AF=8, ACS=8)				
	Pattern	Method	RLNE	PSNR	SSIM
	T2 weighted	JSENSE	36.85 \pm 4.45	21.66 \pm 1.51	73.39 \pm 4.36
pFISTA-SENSE		18.07 \pm 4.13	27.96 \pm 1.79	87.55 \pm 2.42	
MoDL		15.92 \pm 1.35	28.92 \pm 1.36	90.54 \pm 1.27	
Joint-ICNet		16.49 \pm 2.01	28.64 \pm 1.82	89.33 \pm 2.41	
HDLSR		14.94 \pm 1.68	29.49 \pm 1.67	90.41 \pm 1.53	
T2 FLAIR	JDSI	13.52\pm2.25	30.42\pm1.82	91.43\pm2.19	
	JSENSE	24.20 \pm 3.04	23.63 \pm 1.97	79.89 \pm 3.35	
	pFISTA-SENSE	18.86 \pm 3.06	25.84 \pm 2.57	85.92 \pm 2.96	
	MoDL	13.41 \pm 2.65	28.87 \pm 1.44	90.00 \pm 1.70	
	Joint-ICNet	8.08 \pm 1.42	33.23 \pm 2.19	93.73 \pm 1.84	
T2 FLAIR	HDLSR	8.91 \pm 1.50	32.37 \pm 1.97	91.88 \pm 1.83	
	JDSI	7.22\pm1.53	34.28\pm2.88	93.86\pm1.75	
	2D random undersampling pattern (AF=10, ACS=8)				
	T2 FLAIR	pFISTA-SENSE	8.41 \pm 1.49	32.89 \pm 1.56	92.45 \pm 1.58
		MoDL	6.15 \pm 1.08	35.61 \pm 1.58	94.99 \pm 0.89
Joint-ICNet		5.93 \pm 0.98	35.90 \pm 2.10	95.66 \pm 1.39	
HDLSR		5.94 \pm 1.04	35.91 \pm 1.98	95.07 \pm 1.25	
JDSI		5.05\pm0.93	37.34\pm2.05	95.84\pm1.18	

Note: The means and standard deviations are computed over all test data, respectively. The lowest RLNE, highest PSNR and SSIM values are bold faced.

TABLE II

RLNE ($\times 10^{-2}$)/PSNR (dB)/SSIM ($\times 10^{-2}$) OF BRAIN RECONSTRUCTIONS UNDER CALIBRATIONLESS UNDERSAMPLING PATTERNS [MEAN \pm STD].

1D Cartesian undersampling pattern (AF=4)				
Dataset	Method	RLNE	PSNR	SSIM
T2 FLAIR	P-LORAKS	9.22 \pm 1.64	32.08 \pm 2.24	91.38 \pm 1.45
	SAKE	9.02 \pm 1.90	32.33 \pm 2.17	91.40 \pm 2.32
	HDLSR	4.95 \pm 0.90	37.51 \pm 2.07	96.12 \pm 1.08
	JDSI	4.33\pm0.86	38.69\pm2.16	97.15\pm0.83
2D random undersampling pattern (AF=8)				
T2 FLAIR	P-LORAKS	10.99 \pm 1.53	30.50 \pm 2.14	87.79 \pm 2.04
	SAKE	9.47 \pm 1.86	31.89 \pm 2.30	88.83 \pm 2.94
	HDLSR	5.94 \pm 0.97	35.89 \pm 1.92	95.14 \pm 1.20
	JDSI	4.95\pm0.90	37.51\pm2.07	96.12\pm1.08

Note: The means and standard deviations are computed over all test data, respectively. The lowest RLNE, highest PSNR and SSIM values are bold faced.

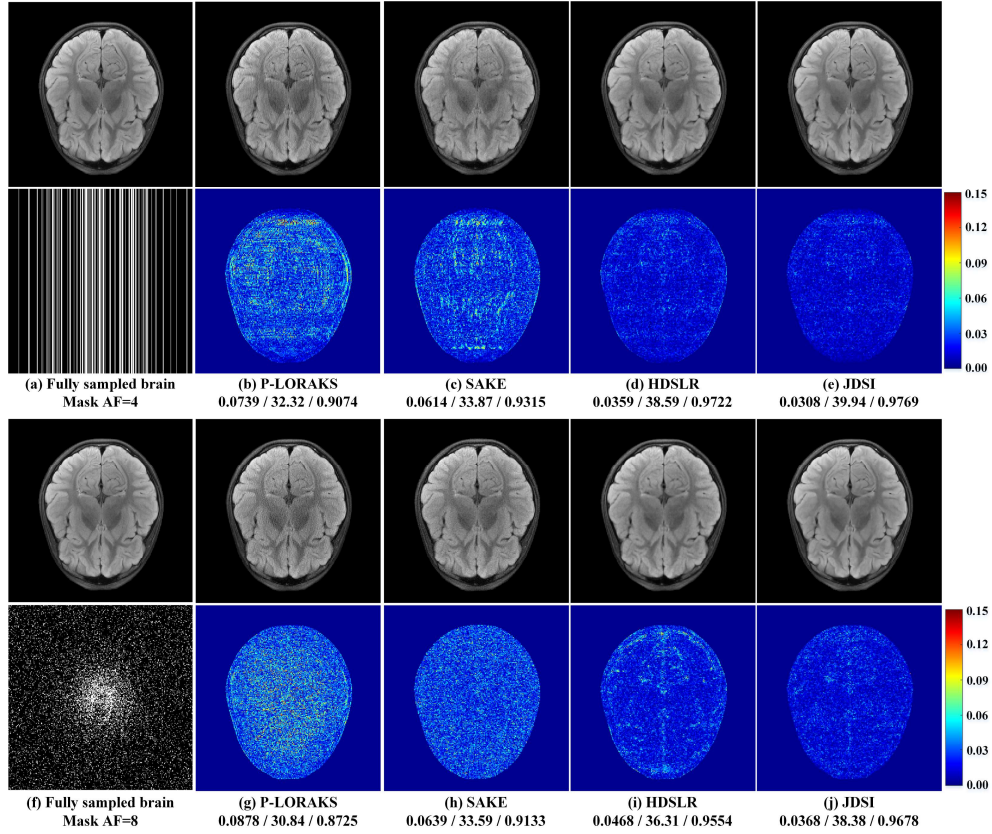


Fig. 5. Calibrationless reconstruction results of the T2 FLAIR brain dataset using different methods. (a) (or (f)) is the fully sampled image and the corresponding undersampling pattern. (b)-(e) (or (g)-(j)) are reconstructed images and the corresponding error maps. Note: RLNE/PSNR(dB)/SSIM are listed for each reconstruction.

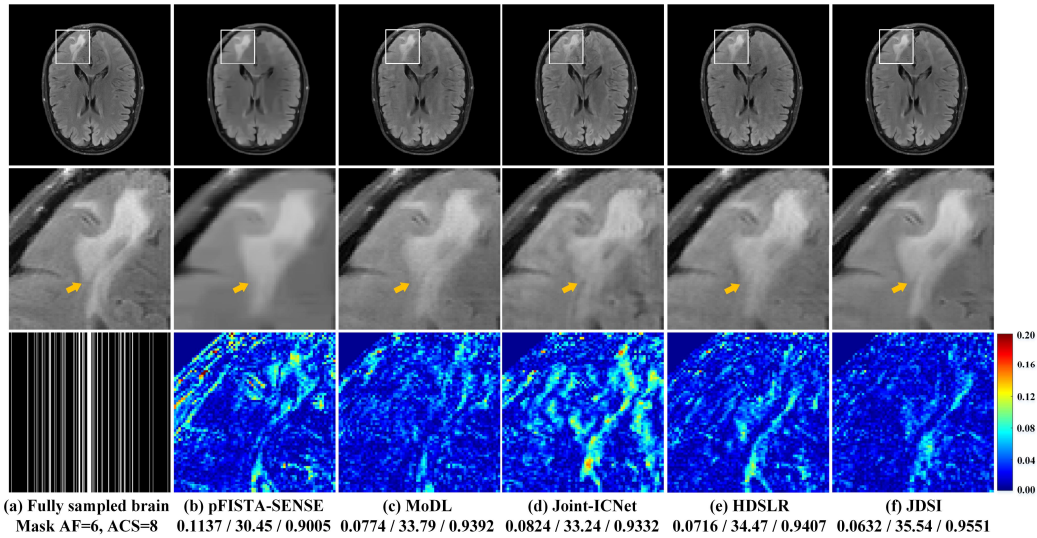


Fig. 6. Reconstruction results of the T2 FLAIR brain dataset with lesion using different methods. (a) (or (f)) is the fully sampled image, magnified details, and the corresponding undersampling pattern. (b)-(f) are reconstructed images, magnified details, and the corresponding error maps. Note: The white matter lesions are marked with yellow arrows. RLNE/PSNR(dB)/SSIM are listed for each reconstruction.

V. DISCUSSIONS

A. Robustness to Abnormal Subjects

In general, the training datasets are mainly composed of healthy volunteers, because they are relatively easy to conduct large-scale acquisition. However, the data of patients are often

different from that of healthy subjects, mainly reflected in the distribution and intensity of abnormal tissues. These differences between the training and target data may lead to the performance drop of deep learning methods. Thus, exploring the robustness of the proposed method to abnormal subjects is essential for clinical applications.

Here, we used a brain dataset of healthy subjects to train all deep learning methods, then to reconstruct a brain image with white matter lesion. Figs. 6(a) and (f) show that the proposed JDSI recovered the abnormal tissues (Marked with yellow arrows) most like the fully sampled image. Whereas other compared methods not recover the lesion well, resulting in over-smooth (Fig. 6(b)), structure loss (Fig. 6(c)), intensity loss (Fig. 6(d)), and residual artifacts (Fig. 6(e)).

The observation demonstrates that the proposed JDSI owns some robustness to abnormal subjects.

B. Robustness to Different ACS Lines

The ACS is crucial for accelerated MRI reconstruction, once the number of ACS lines is limited, the pre-estimated sensitivity maps become inaccurate, leading to the degradation of reconstruction [12, 14]. Thus, refining sensitivity maps during the reconstruction may be important.

Here, to validate the effectiveness of our joint network, we compared the proposed JDSI with other two methods that pre-estimate the sensitivity maps using JSENSE [12] and ESPIRiT [6], named as JDSI-JSENSE and JDSI-ESPIRiT, respectively. The network architectures of latter two are consistent with JDSI, except for removing the sensitivity-update-related modules.

Fig. 7 shows that, for the tested number of ACS lines, the proposed JDSI consistently outperforms other two methods in terms of three evaluation criteria. Moreover, with a decrease of ACS lines (<16 lines), the accuracy of two pre-estimated sensitivity maps decreases, resulting in significant evaluation criteria degradations in JDSI-JSENSE and JDSI-ESPIRiT. By updating the sensitivity maps in the network, these criteria of the proposed JDSI are only slightly reduced when the ACS lines are reduced. Thus, updating the sensitivity maps provides robustness to ACS lines.

Representative images in Figs. 8(a)-(d) show that, when ACS lines are enough (ACS=24), all three methods can yield good sensitivity estimations and suppress artifacts well. The sensitivity map of JDSI is closest to ground truth due to sensitivity refinement. However, when the ACS lines are limited (Figs. 8(e)-(h)), JSENSE and ESPIRiT provide inferior sensitivity maps, resulting in obvious artifacts in reconstructed images, whereas our JDSI provides consistently superior sensitivity estimation with nice image artifacts suppression.

It demonstrates the importance of the faithful sensitivity estimation for high-quality image reconstructions. Our joint network overcomes the limitation of conventional sensitivity estimation strategies under limited ACS lines, providing high-quality and robust reconstructions.

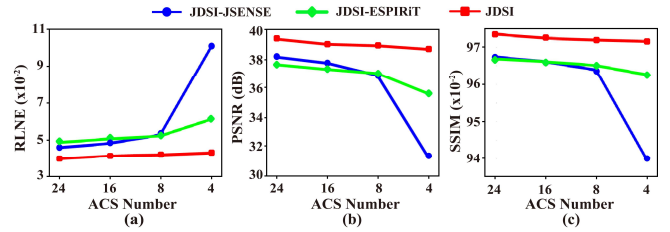


Fig. 7. Quantitative comparison of reconstructions using different methods with different number of ACS lines of a brain dataset. (a)-(c) are the mean of RLNE, PSNR, SSIM of the reconstructions, respectively. Note: The 1D Cartesian undersampling pattern with AF=4 is used. The difference between each mask is the number of ACS lines. The means are computed over all test data.

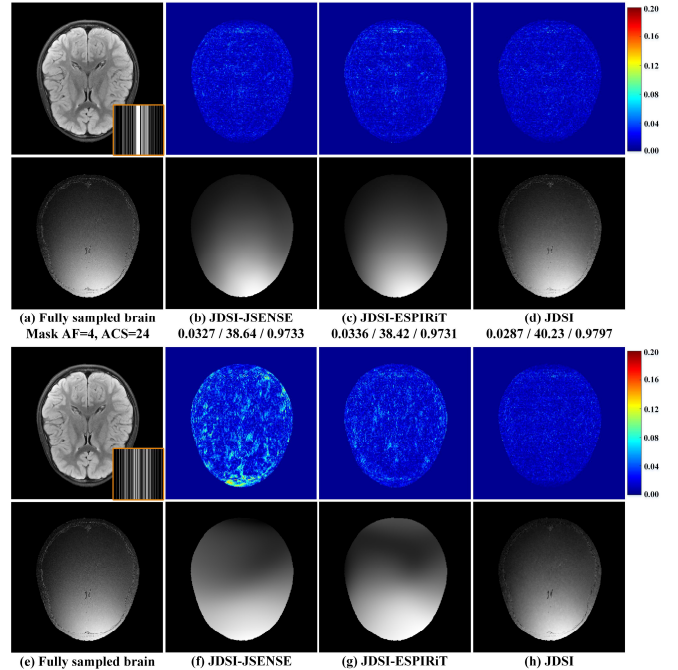


Fig. 8. Reconstructed brain images with and without enough ACS lines. (a) (or (e)) is the fully sampled image, the corresponding undersampling pattern, and the ground truth sensitivity map of 14th coil. (b)-(d) (or (f)-(h)) are reconstruction errors and estimated sensitivity maps. Note: The 1D Cartesian undersampling patterns are used. RLNE/PSNR/(dB)/SSIM are listed for each reconstruction.

C. Reader Study

Since objective criteria (i.e., RLNE, PSNR, and SSIM) might not reflect image quality in terms of diagnostically important features, we further invited three radiologists (with 12, 29, and 30 years of clinical experience) to independently evaluate the reconstruction images. They were blind to the reconstruction methods. To avoid rater bias, the order of reconstructed images

TABLE III
THE SCORES AND P-VALUES OF THE READER STUDY. [MEAN±STD]

Criterion	MoDL	Joint-ICNet	HDSLRL	JDSI	P-value of JDSI versus		
					MoDL	Joint-ICNet	HDSLRL
Signal-to-noise ratio	3.59±0.30	3.72±0.22	3.51±0.15	4.01±0.19	3.55e-11	3.94e-10	1.59e-11
Artifacts suppression	3.65±0.44	3.59±0.27	3.52±0.15	4.01±0.18	3.41e-10	1.94e-11	2.35e-11
Overall image quality	3.64±0.29	3.70±0.20	3.53±0.15	4.02±0.18	3.84e-11	5.28e-11	1.67e-11

Note: There are 60 slices from 10 healthy subjects and 10 abnormal subjects used for reader study. The means and standard deviations are computed over all images, respectively. P-value < 0.01 indicates the differences between two compared methods are great significant. The highest scores are bold faced.

was presented randomly for each slice. Three clinical concerned criteria including signal-to-noise ratio, artifacts suppression, and overall image quality were used. The score of each criterion had a range from 0 to 5 with precision of 0.1 (i.e., 0~1: Non-diagnostic; 1~2: Poor; 2~3: Adequate; 3~4: Good; 4~5: Excellent). The reader study was conducted online through our Cloud Brain Imaging platform [22, 38] at <https://csrc.xmu.edu.cn/CloudBrain.html>.

The images used for reader study were axial T2 FLAIR images reconstructed under the 1D Cartesian undersampling pattern with AF=6. They included 10 healthy subjects and 10 abnormal subjects. To reduce the burden of radiologists' scoring, each subject contained about central 3 slices which have sufficient tissue information.

Table III shows that, the proposed JDSI obtains highest mean scores. It is the only one which all three criteria are slightly over 4, indicating the reconstructed images are suitable for diagnosis. These results are consistent to the superiority of JDSI on above-mentioned objective criteria. The scores of other compared methods mean their images are good for diagnosis. Besides, the differences between JDSI and other compared methods are great significant according to all P-values of the Wilcoxon signed rank test < 0.01 .

In summary, the image quality improvements obtained by the proposed JDSI is significant and the overall quality steps into the excellent level for clinical diagnosis.

VI. CONCLUSION

In this work, we present a Joint Deep Sensitivity estimation and Image reconstruction network (JDSI) for accelerated magnetic resonance imaging (MRI). Our network simultaneously achieves the faithful estimation of sensitivity maps and the reconstruction of high-quality images. Extensive results on *in vivo* datasets and radiologist reader study demonstrate that, the proposed JDSI provides improved and more robust reconstruction performance than state-of-the-art methods, especially when the acquisition is highly accelerated.

ACKNOWLEDGMENTS

The authors thank Yirong Zhou and Jiayu Li for supporting the reader study on the Cloud Brain Imaging platform; Xinlin Zhang for the helpful discussions; Weiping He, Shaorong Fang, and Tianfu Wu from Information and Network Center of Xiamen University for the help with the GPU computing; Drs. Michael Lustig, Mathews Jacob, and Justin P. Haldar for sharing their codes online.

REFERENCES

- [1] G. H. Mukesh, A. O'Shea, and R. Weissleder, "Advances in clinical MRI technology," *Sci. Transl. Med.*, vol. 11, no. 523, eaba2591, 2019.
- [2] M. Lustig, D. Donoho, and J. M. Pauly, "Sparse MRI: The application of compressed sensing for rapid MR imaging," *Magn. Reson. Med.*, vol. 58, no. 6, pp. 1182-1195, 2007.
- [3] K. P. Pruessmann, M. Weiger, M. B. Scheidegger, and P. Boesiger, "SENSE: Sensitivity encoding for fast MRI," *Magn. Reson. Med.*, vol. 42, no. 5, pp. 952-962, 1999.
- [4] M. A. Griswold *et al.*, "Generalized autocalibrating partially parallel acquisitions (GRAPPA)," *Magn. Reson. Med.*, vol. 47, no. 6, pp. 1202-1210, 2002.
- [5] Z. Liang, "Spatiotemporal imaging with partially separable functions," in *4th IEEE International Symposium on Biomedical Imaging (ISBI)*, 2007, pp. 988-991.
- [6] M. Uecker *et al.*, "ESPIRiT—An eigenvalue approach to autocalibrating parallel MRI: Where SENSE meets GRAPPA," *Magn. Reson. Med.*, vol. 71, no. 3, pp. 990-1001, 2014.
- [7] S. Ravishanker and Y. Bresler, "MR image reconstruction from highly undersampled k-space data by dictionary learning," *IEEE Trans. Med. Imaging*, vol. 30, no. 5, pp. 1028-1041, 2011.
- [8] M. Guerquin-Kern, M. Haberlin, K. P. Pruessmann, and M. Unser, "A fast wavelet-based reconstruction method for magnetic resonance imaging," *IEEE Trans. Med. Imaging*, vol. 30, no. 9, pp. 1649-1660, 2011.
- [9] X. Qu, Y. Hou, F. Lam, D. Guo, J. Zhong, and Z. Chen, "Magnetic resonance image reconstruction from undersampled measurements using a patch-based nonlocal operator," *Med. Image Anal.*, vol. 18, no. 6, pp. 843-856, 2014.
- [10] Y. Liu, Z. Zhan, J.-F. Cai, D. Guo, Z. Chen, and X. Qu, "Projected iterative soft-thresholding algorithm for tight frames in compressed sensing magnetic resonance imaging," *IEEE Trans. Med. Imaging*, vol. 35, no. 9, pp. 2130-2140, 2016.
- [11] X. Zhang *et al.*, "A guaranteed convergence analysis for the projected fast iterative soft-thresholding algorithm in parallel MRI," *Med. Image Anal.*, vol. 69, pp. 101987, 2021.
- [12] L. Ying and J. Sheng, "Joint image reconstruction and sensitivity estimation in SENSE (JSENSE)," *Magn. Reson. Med.*, vol. 57, no. 6, pp. 1196-1202, 2007.
- [13] M. Lustig and J. M. Pauly, "SPIRiT: Iterative self-consistent parallel imaging reconstruction from arbitrary k-space," *Magn. Reson. Med.*, vol. 64, no. 2, pp. 457-471, 2010.
- [14] P. J. Shin *et al.*, "Calibrationless parallel imaging reconstruction based on structured low-rank matrix completion," *Magn. Reson. Med.*, vol. 72, no. 4, pp. 959-970, 2014.
- [15] K. H. Jin, D. Lee, and J. C. Ye, "A general framework for compressed sensing and parallel MRI using annihilating filter based low-rank Hankel matrix," *IEEE Trans. Comput. Imaging*, vol. 2, no. 4, pp. 480-495, 2016.
- [16] J. P. Haldar and J. Zhuo, "P-LORAKS: Low-rank modeling of local k-space neighborhoods with parallel imaging data," *Magn. Reson. Med.*, vol. 75, no. 4, pp. 1499-1514, 2016.
- [17] X. Zhang *et al.*, "Image reconstruction with low-rankness and self-consistency of k-space data in parallel MRI," *Med. Image Anal.*, vol. 63, pp. 101687, 2020.
- [18] X. Zhang *et al.*, "Accelerated MRI reconstruction with separable and enhanced low-rank Hankel regularization," *IEEE Trans. Med. Imaging*, vol. 41, no. 9, pp. 2486-2498, 2022.
- [19] S. Wang *et al.*, "Accelerating magnetic resonance imaging via deep learning," in *IEEE 13th International Symposium on Biomedical Imaging (ISBI)*, 2016, pp. 514-517.
- [20] B. Zhu, J. Z. Liu, S. F. Cauley, B. R. Rosen, and M. S. Rosen, "Image reconstruction by domain-transformation manifold learning," *Nature*, vol. 555, no. 7697, pp. 487-492, 2018.
- [21] Y. Yang, J. Sun, H. Li, and Z. Xu, "ADMM-CSNet: A deep learning approach for image compressive sensing," *IEEE Trans. Pattern Anal. Mach. Intell.*, vol. 42, no. 3, pp. 521-538, 2020.
- [22] Q. Yang, Z. Wang, K. Guo, C. Cai, and X. Qu, "Physics-driven synthetic data learning for biomedical magnetic resonance: The imaging physics-based data synthesis paradigm for artificial intelligence," *IEEE Signal Process. Mag.*, DOI: 10.1109/MSP.2022.3183809, 2022.
- [23] Y. Han, L. Sunwoo, and J. C. Ye, "k-space deep learning for accelerated MRI," *IEEE Trans. Med. Imaging*, vol. 39, no. 2, pp. 377-386, 2020.
- [24] A. Pramanik, H. Aggarwal, and M. Jacob, "Deep generalization of structured low-rank algorithms (Deep-SLR)," *IEEE Trans. Med. Imaging*, vol. 39, no. 12, pp. 4186-4197, 2020.
- [25] Z. Wang *et al.*, "One-dimensional deep low-rank and sparse network for accelerated MRI," *IEEE Trans. Med. Imaging*, DOI: 10.1109/TMI.2022.3203312, 2022.
- [26] K. Hammernik *et al.*, "Learning a variational network for reconstruction of accelerated MRI data," *Magn. Reson. Med.*, vol. 79, no. 6, pp. 3055-3071, 2018.
- [27] H. K. Aggarwal, M. P. Mani, and M. Jacob, "MoDL: Model-based deep learning architecture for inverse problems," *IEEE Trans. Med. Imaging*, vol. 38, no. 2, pp. 394-405, 2019.
- [28] T. Lu *et al.*, "pFISTA-SENSE-ResNet for parallel MRI reconstruction," *J. Magn. Reson.*, vol. 318, pp. 106790, 2020.

-
- [29] L. Bao *et al.*, “Undersampled MR image reconstruction using an enhanced recursive residual network,” *J. Magn. Reson.*, vol. 305, pp. 232-246, 2019.
 - [30] X. Peng, B. P. Sutton, F. Lam, and Z.-P. Liang, “DeepSENSE: Learning coil sensitivity functions for SENSE reconstruction using deep learning,” *Magn. Reson. Med.*, vol. 87, no. 4, pp. 1894-1902, 2022.
 - [31] A. Sriram *et al.*, “End-to-End variational networks for accelerated MRI reconstruction,” in *Medical Image Computing and Computer Assisted Intervention (MICCAI)*, 2020, pp. 64-73.
 - [32] Y. Jun, H. Shin, T. Eo, and D. Hwang, “Joint deep model-based MR image and coil sensitivity reconstruction network (Joint-ICNet) for fast MRI,” in *IEEE Conference on Computer Vision and Pattern Recognition (CVPR)*, 2021, pp. 5270-5279.
 - [33] J. Zhang and B. Ghanem, “ISTA-Net: Interpretable optimization-inspired deep network for image compressive sensing,” in *IEEE Conference on Computer Vision and Pattern Recognition (CVPR)*, 2018, pp. 1828-1837.
 - [34] Z. Wang *et al.*, “A sparse model-inspired deep thresholding network for exponential signal reconstruction--Application in fast biological spectroscopy,” *IEEE Trans. Neural Netw. Learn. Syst.*, DOI: 10.1109/TNNLS.2022.3144580, 2022.
 - [35] O. Ronneberger, P. Fischer, and T. Brox, “U-Net: Convolutional networks for biomedical image segmentation,” in *Medical Image Computing and Computer-Assisted Intervention (MICCAI)*, 2015, pp. 234-241.
 - [36] F. K. Zbontar *et al.*, “FastMRI: An open dataset and benchmarks for accelerated MRI,” arXiv: 1811.08839, 2019.
 - [37] W. Zhou, A. C. Bovik, H. R. Sheikh, and E. P. Simoncelli, “Image quality assessment: From error visibility to structural similarity,” *IEEE Trans. Image Process.*, vol. 13, no. 4, pp. 600-612, 2004.
 - [38] Y. Zhou *et al.*, “XCloud-pFISTA: A medical intelligence cloud for accelerated MRI,” in *43rd Annual International Conference of the IEEE Engineering in Medicine & Biology Society (EMBC)*, 2021, pp. 3289-3292.